Earth and Planetary Science Letters 539 (2020) 116226

Contents lists available at ScienceDirect

Earth and Planetary Science Letters

www.elsevier.com/locate/epsl

Coseismic damage runs deep in continental strike-slip faults

Bo Ra Song *, Scott E. Johnson, Won Joon Song, Cristopher C. Gerbi, Martin G. Yates

School of Earth and Climate Sciences, University of Maine, Orono, ME 04469, USA

ARTICLE INFO

Article history:
Received 23 October 2019
Received in revised form 5 March 2020
Accepted 12 March 2020
Available online 27 March 2020
Editor: R. Bendick

Keywords:
fault zone damage
asymmetric damage
dynamic fragmentation
frictional-to-viscous transition
power-law distribution
garnet

ABSTRACT

Coseismic off-fault damage and pulverization significantly influence the mechanical and transport properties, and in turn the rupture dynamics of faults. Although field-based, laboratory, and numerical studies help elucidate the structure of damage zones adjacent to modern strike-slip faults, the vertical extent of these zones remains an open question. To address this question, we analyzed particle size distribution and microfracture density of fragmented garnets from the Sandhill Corner shear zone, a strand of an ancient, seismogenic, strike-slip fault system exhumed from frictional-to-viscous transition depths (400–500 °C). The shear zone has mutually overprinting pseudotachylyte and mylonite, and juxtaposes quartzofeldspathic and schist units. The inner parts of the quartzofeldspathic and schist units (∼63 m and ∼5 m wide from the lithologic contact, respectively) have two-dimensional *D*-values ≥1.5, which indicates dynamic fragmentation during rupture propagation. Similar to the particle size distribution analysis, microfracture density data from the garnets show progressive but asymmetric increase toward the core in each unit. Our results suggest that coseismic damage extends down to the base of the seismogenic zone in mature strike-slip faults, and the asymmetric distribution of damage may indicate preferred rupture directivity as proposed for some modern strike-slip faults.

1. Introduction

Highly fractured and pulverized rocks are common in damage zones adjacent to active or recently active seismogenic strike-slip faults (e.g., Rockwell et al., 2009; Mitchell et al., 2011; Wechsler et al., 2011; Morton et al., 2012; Rempe et al., 2013; Muto et al., 2015). Field-based geological data, geophysical data, laboratory experiments, and numerical simulations have helped to elucidate the structure and spatial extent of coseismic damage zones (e.g., Cochran et al., 2009; Yuan et al., 2011; Sagy and Korngreen, 2012; Xu and Ben-Zion, 2017). However, the maximum depth to which this dynamic damage occurs, and the width of the resulting damage zones at depth, remain open questions. Based on evidence from field observations, Aben et al. (2017) suggested that pulverization can extend to a depth of ∼10 km or less. On the other hand, recent analysis of past earthquakes in southern California estimated the production of rock damage at a depth of 10–15 km (Ben-Zion and Zaliapin, 2019), and Incel et al. (2019) found experimental evidence for pulverization of garnet at upper mantle depths. Studies from exhumed seismogenic shear zones also documented the occurrence of pulverization at middle and lower crustal depths in thrust (e.g., Trepmann and Stöckhert, 2002; Jamtveit et al., 2019), normal (e.g., Soda and Okudaira, 2018), and strike-slip fault systems (e.g., Sullivan and Peterman, 2017). However, there has not been a systematic study of the lateral extent of coseismic rock damage at the base of mature strike-slip faults.

Damage zones significantly change the mechanical properties of rocks and reduce seismic velocities (e.g., Walsh, 1965; Lockner et al., 1977; Cochran et al., 2009). Seismic waves trapped in low velocity damage zones can produce complex pattern of slip and rupture propagation such as oscillations of stick-slip behavior, short rise-time pulse-like rupture, and supershear rupture, as well as amplifying near-fault ground motion (e.g., Harris and Day, 1997; Spudich and Olsen, 2001; Huang et al., 2014). Therefore, the width and depth extent of damage zones is fundamentally important for assessing seismic hazard. Damage zones at depth also influence transient and long-term changes in fluid flow (e.g., Mitchell and Faulkner, 2012), heat transport (e.g., Morton et al., 2012), and overall fault rock rheology (e.g., Handy et al., 2007).

This paper provides measurements of particle size distribution (PSD) and fracture density for fragmented garnets across an ancient seismogenic strike-slip fault/shear zone exhumed from depths corresponding to temperatures of 400–500 °C (∼13–17 km if the geothermal gradient was 30 °C/km), and we use these data to define the lateral extent of high-energy dynamic deformation. Several studies inferred damage related to the seismogenic cycle at depth based on deformation microstructure in quartz (e.g., Trepmann et al., 2007; Price et al., 2016). However, quartz at these

* Corresponding author.
E-mail address: bora.song@maine.edu (B.R. Song).

https://doi.org/10.1016/j.epsl.2020.116226
0012-821X/

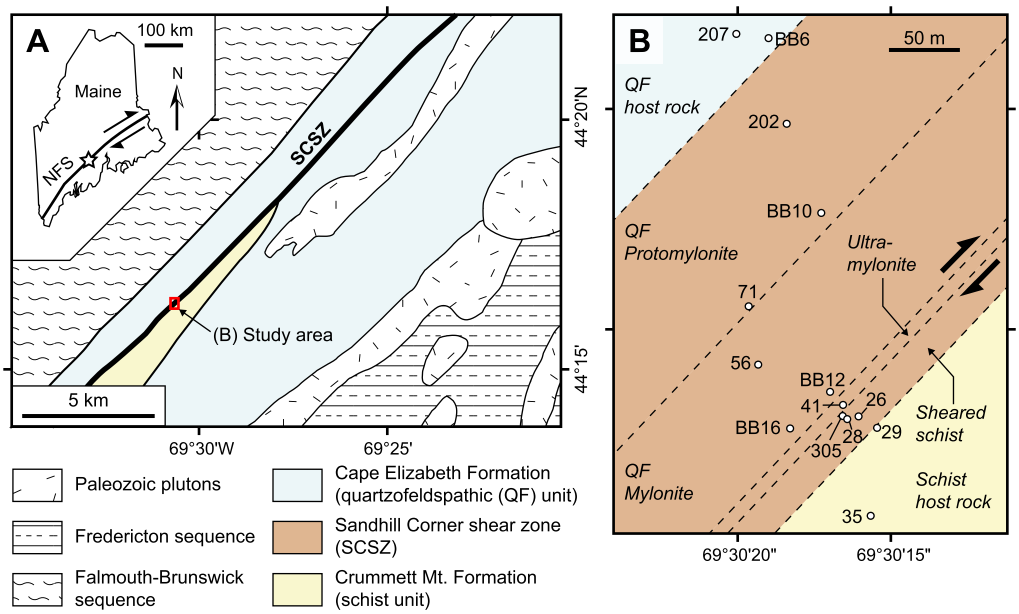

Fig. 1. Geologic maps of the Sandhill Corner shear zone (SCSZ) in the Norumbega fault system (NFS). Modified from Price et al. (2016). (A) Regional geologic setting of the study area. The SCSZ is located in the central part of the NFS (denoted by a star in the inset map of Maine, USA). The red box indicates the study area. (B) Study area and sample locations. The core of the shear zone (ultramylonite) is the lithologic contact between quartzofeldspathic (QF) and schist units. White dots correspond to sample locations, and paired arrows indicate shear sense. See the online article for the color version of this figure.

temperatures deforms by both brittle and viscous processes that overprint one another during co-, post- and interseismic cycles, and the mutually overprinting deformation mechanisms can obscure the record of brittle coseismic damage. Garnet, in contrast, does not deform viscously at such low temperatures, and so can preserve coseismic microfractures in the deeper reaches of the seismogenic zone (e.g., Jamtveit et al., 2019). Thus, PSD and fracture density of garnet across the fault/shear zone may provide convincing evidence for coseismic damage and pulverization, and allow characterization of the spatial gradient and extent of the damage as a function of distance from the shear zone core. We also calculated fabric intensity (using M-index; Skemer et al., 2005) of fragmented garnets to obtain information about their post-fragmentation rotation caused by viscous flow of the surrounding matrix during post- and interseismic cycles.

The microstructures of fragmented garnet have been used to infer coseismic damage at frictional-to-viscous transition (FVT) depths (at temperatures of ∼300–350 °C; Trepmann and Stöckhert, 2002) and in the deeper crust (corresponding to temperatures of 650–700 °C; Jamtveit et al., 2019). Feldspar fragmentation has also been reported at FVT depths (>400 °C; Sullivan and Peterman, 2017) and in the deeper crust (∼600–750 °C; Soda and Okudaira, 2018). However, most of these studies did not present PSD analysis, which has been widely used to infer high-energy dynamic processes in the brittle upper crust (e.g., Rockwell et al., 2009; Wechsler et al., 2011; Buhl et al., 2013; Hossain and Kruhl, 2015; Muto et al., 2015). Fracturing of brittle minerals (e.g., garnet) hosted in a ductile matrix is not uncommon in foliated metamorphic rocks (e.g., Ji et al., 1997), and can be caused by quasi-static deformation processes. However, at dynamic stresses with increasing energy, the relative abundance of smaller fragments increases, while the relative abundance of larger fragments decreases (e.g., Muto et al., 2015 and references therein). Thus, the PSD resulting from dynamic fragmentation is distinct from that resulting from quasi-static processes, and therefore a slope in a cumulative log–log plot of PSD (see Section 3) can be used to infer the process of fragmentation. Soda and Okudaira (2018) used PSDs of fine-grained feldspar, but the study of fragmented feldspar is more challenging because its fracturing can be controlled by cleavage, possibly leading to significant directional anisotropy in the microfractures. Jamtveit et al. (2019) analyzed PSDs of fragmented garnets around pseudotachylyte veins and documented cm-wide damage zones. Here, we describe garnet fragmentation using PSD analysis at the base of a mature strike-slip fault (the Sandhill Corner shear zone) in an attempt to define the spatial extent of off-fault damage and pulverization.

2. The Sandhill Corner shear zone (SCSZ)

The northeast-trending SCSZ is the longest continuous strand of the Norumbega fault system, which is a Paleozoic, crustal-scale, large-displacement, right-lateral strike-slip fault system in the northern Appalachians, USA (Fig. 1). A kinematic vorticity number of 0.97 in the SCSZ was reported by Johnson et al. (2009), indicating approximately strike-slip flow (subsimple shear). The ∼230 m-wide shear zone consists of a quartzofeldspathic (QF) unit (protomylonite to mylonite) and a sheared schist unit. The shear zone core is a ∼5 m-wide zone of ultramylonite/phyllonite rock, containing abundant deformed and undeformed pseudotachylyte veins (locally >50% of rock volume), and coincident with the lithologic contact between the QF and schist units (Figs. 2A and 2B; Price et al., 2012). The SCSZ, especially within the immediate vicinity of the core, preserves evidence for the mutual overprinting of pseudotachylyte and mylonite (Price et al., 2012), which reflects coeval frictional and viscous deformation during seismogenic cycles (e.g., Handy et al., 2007). Based on quartz (dislocation creep and subgrain rotation recrystallization) and feldspar (fracturing) deformation, Price et al. (2016) estimated that mylonitic deformation, overprinting previous higher-temperature microstructures outside the shear zone, occurred at temperatures of 400–500 °C. Plagioclase in and near the core displays multiple generations of microfractures and fragmentation down to submicron scale with little or no internal strain (Figs. 2C, 2D and 2E). Garnet is fragmented in various styles: intact, split into several pieces, and partially and pervasively fractured. Some fragmented garnets within and near the core underwent moderate to extreme post-fragmentation shearing and stretching, leading to aspect ratios of the fragment mass exceeding 8 (e.g., sample BB16 in Fig. 3).

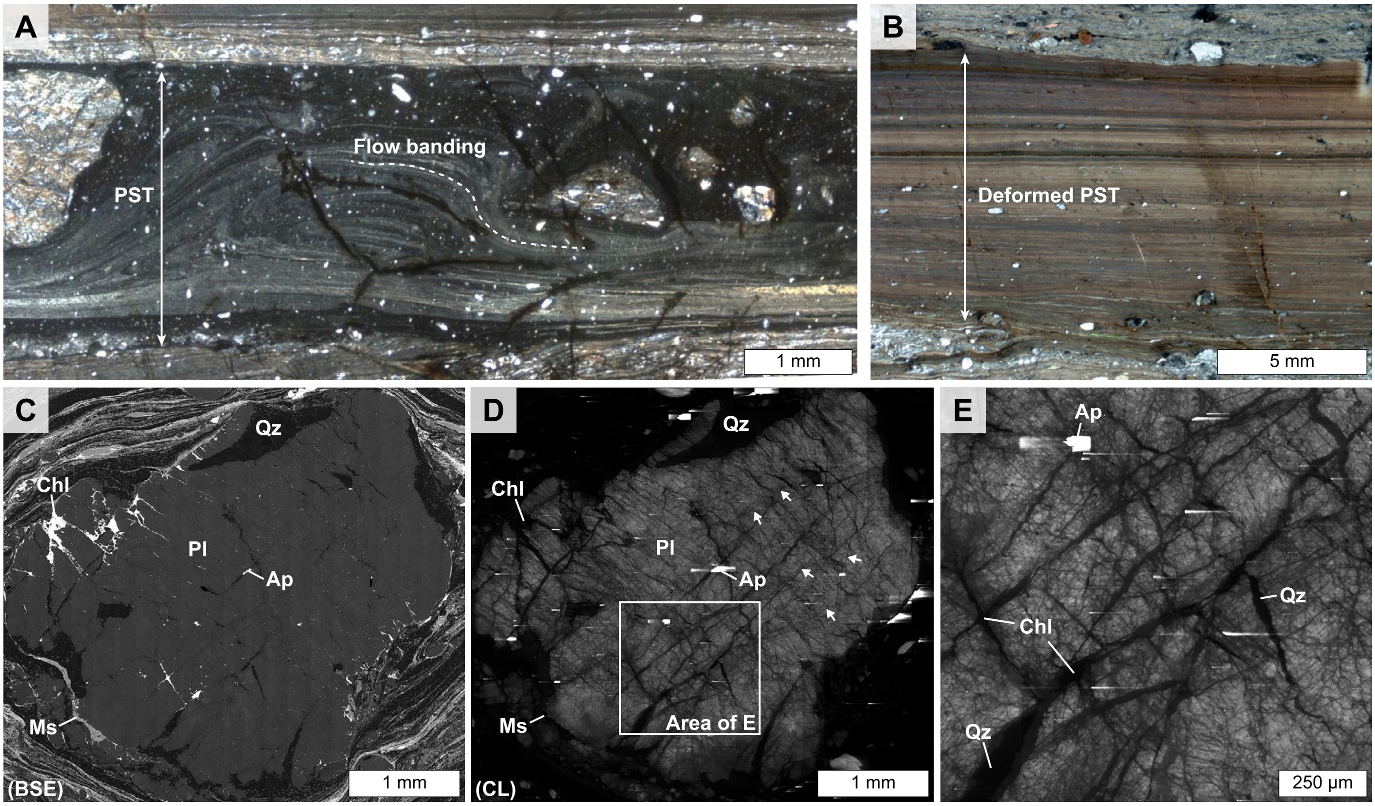

Fig. 2. Rock microstructures in or near the shear zone core. (A) Photomicrograph (cross-polarized light) of undeformed pseudotachylytes (PST). The undeformed PST contains flow banding (dashed curve) that shows melt flow structure. (B) Photomicrograph (cross-polarized light) of deformed PST. Internal layers of the deformed PST are generally concordant with the external mylonitic foliation of the shear zone. (C) Backscattered electron (BSE) image of shattered plagioclase in the QF mylonite near the shear zone core. Microfractures are partly filled with quartz, chlorite and apatite. (D) Cathodoluminescence (CL) image of (C). Healed microfracture networks appear as dark CL bands (arrows). (E) CL image of area outlined in (D) showing extreme fragmentation. Micron and submicron-sized fragments are observed. Mineral abbreviations are: Ap = apatite, Chl = chlorite, Ms = Muscovite, Pl = plagioclase, Qz = quartz. See the online article for the color version of this figure.

3. Methods

We analyzed 15 thin-sections of garnet-bearing rock samples across the SCSZ (Fig. 1B). The rock samples were cut perpendicular to the main foliation and parallel to the stretching lineation (XZ plane), except one sample (BB16-a) that was cut perpendicular to both foliation and lineation (YZ plane). All the sections were polished mechanically with 0.3 µm alumina suspension and chemically in 0.02 µm colloidal silica suspension, and then were coated with a thin layer of carbon to prevent electron charging. They were used to acquire backscattered electron (BSE) images and electron backscatter diffraction (EBSD) maps of garnet from a Tescan Vega II scanning electron microscope at the University of Maine, USA.

We measured two-dimensional PSD of fragmented garnet from BSE images using a technique similar to that reported in Keulen et al. (2007). We selected one highly fragmented garnet from each thin section and collected high-resolution BSE images (4,000× magnification) to cover the whole area of each garnet. We stitched 40 to 426 images, depending on garnet size, to create a single image. For stretched garnets with rotated fragments, we chose to analyze relatively less rotated areas that contain a wide range of fragment sizes (red boxes in Fig. 3) to minimize the effect of post- and interseismic deformation on PSD (see Section 4.2). For segmented bitmap of garnet and its image analysis, we used ImageSXM (https://www.liverpool.ac.uk/~sdb/ImageSXM/) with a macro ('Lazy Erode Dilate'; https://micro.earth.unibas.ch/support/LazyMacros/) and ImageJ (https://imagej.nih.gov/ij/). During ranking filter processes through the macro, the bitmaps were manually modified to maintain the original fragment shapes by comparing with the BSE images. For example, hairline microfractures that could not be automatically identified were manually traced. For sample BB12 which showed unclear fracture lines too thin to identify in the BSE image at 4,000× magnification (especially true for fine fragments <6 µm in that sample), additional BSE images at 10,000× magnification were collected in sub-areas containing fine fragments. Cross-sectional areas of fragments were measured in the processed bitmaps after removing fragments smaller than 20 pixel^2 (equivalent to 0.34 µm and 0.14 µm in size for magnifications of 4,000× and 10,000×, respectively). The number of analyzed fragments in each garnet ranged from ∼200 to ∼12,000. To restore the 'eroded' outline of each fragment during the segmentation, the pixel values equivalent to its perimeter were added to the area. Then, we calculated area-equivalent diameters, which are taken as particle size in our PSD analysis. PSD data are commonly analyzed using a power-law function within a specific range of particle sizes (Mandelbrot, 1982). This power-law relationship can be quantified by the cumulative frequency curve in log–log plot of $N(>d) = kd^{-D}$, where $N(>d)$ is the number of particles greater than diameter d, k is a constant, and the exponent D (D-value in two dimensions here) is the negative slope of a best-fit line over a linear part of the plot (Turcotte, 1986). For comparison purposes, three-dimensional D-values of other studies were converted to two-dimensional D-values by subtracting one (Sammis et al., 1987). On a log(cumulative frequency) – log(size) plot, we used 20 bins per order of magnitude of particle size. In sample BB12, the PSD data from two magnifications were combined into a single plot, multiplying the frequency in each bin at 10,000× magnification by a factor to the particle numbers at 4,000× magnification. To correct for variation in overlapping bins of two magnifications, the average frequency of the overlapping bins is used.

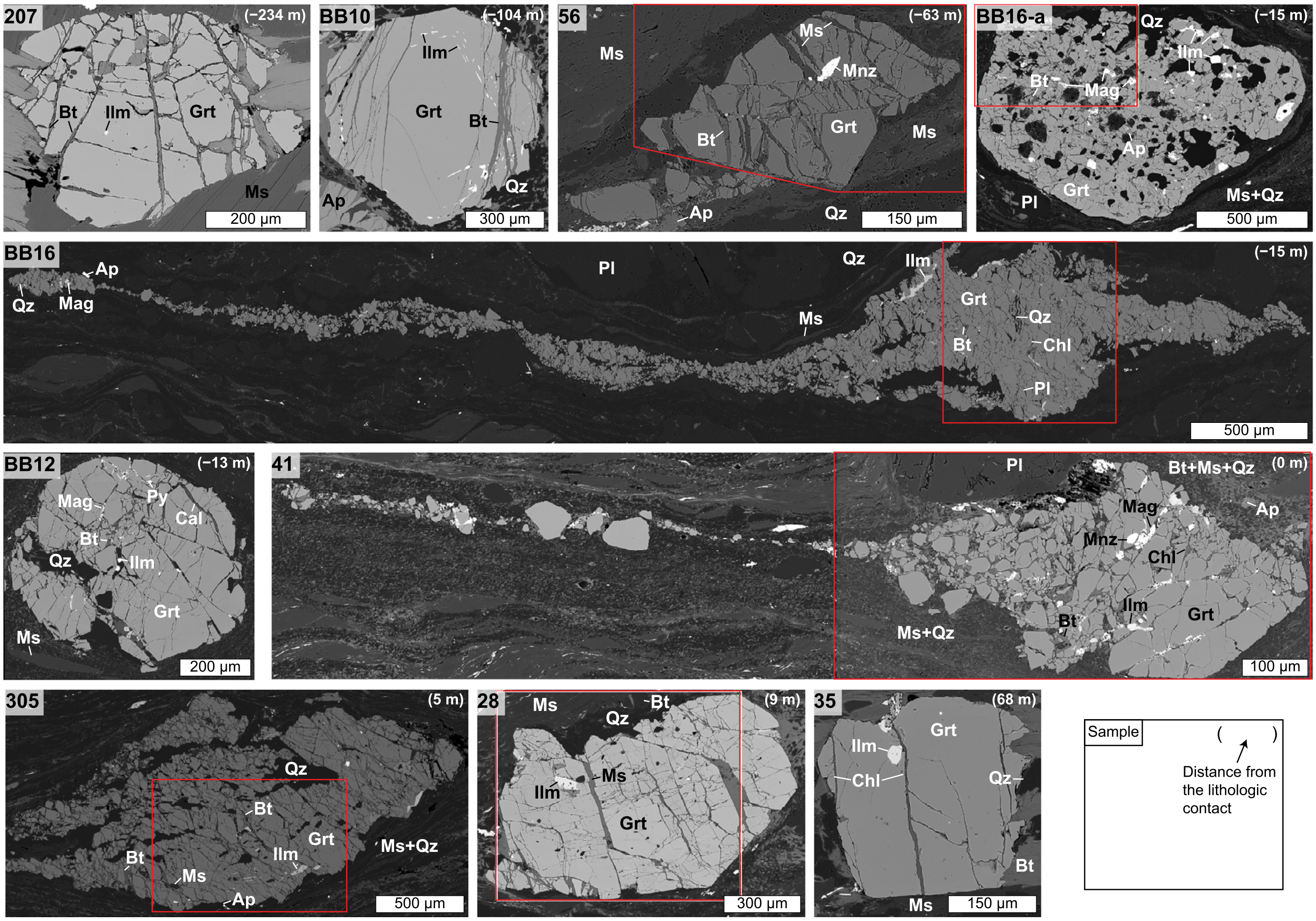

Fig. 3. BSE images of ten representative garnet samples. Red boxes show the analysis areas of particle size distribution (PSD). The images are arranged from the QF host rock, through the shear zone core, to the schist host rock. Perpendicular distance for each sample was measured from the lithologic contact between the QF and schist units, and is shown in the upper-right corner of each image. Negative value of distance indicates the QF area. Note that while garnets in the host rocks and the outer shear zone (samples 207, BB10, 28 and 35) show one or more sets of preferred microfracture orientations, the inner shear zone garnets (samples 56, BB16-a, BB16, BB12, 41 and 305) have a large number of microfractures without preferred orientation. See Fig. S1 for all the analyzed garnet samples. As fracture-filling minerals, quartz, micas (locally chloritized), calcite and feldspar are displayed in gray to dark gray, and oxides, phosphates and sulfides are shown in bright white. Mineral abbreviations are: Ap = apatite, Bt = biotite, Cal = calcite, Chl = chlorite, Grt = garnet, Ilm = ilmenite, Mag = magnetite, Mnz = monazite, Ms = Muscovite, Pl = plagioclase, Py = pyrite, Qz = quartz. See the online article for the color version of this figure.

We also measured microfracture density of garnets in the stitched BSE images through a linear scanline method, widely used to characterize fracture networks (e.g., Anders and Wiltschko, 1994; Mitchell et al., 2011). To minimize the effect of operator sampling bias, we used 8 to 12 randomly oriented scanlines drawn across each garnet (Anders and Wiltschko, 1994). The garnet microfracture density (#/mm) is defined as the total number of microfractures that intersect scanlines divided by the total scanline length. In the case of dilated microfractures separating garnet fragments, the scanline length within each dilated fracture was subtracted from the total scanline length.

EBSD patterns of garnets were collected in an EDAX-TSL EBSD system at an acceleration voltage of 20 kV, a sample tilt of 70°, and a working distance of 25 mm, using a step size between 1 and 2 μm. EDAX-TSL OIM Analysis 6 software was used to construct EBSD maps and obtain misorientation angle distributions. The misorientation index (M-index; Skemer et al., 2005) was calculated to represent fabric intensity of fragmented garnets. The M-index is defined as the difference between the observed distribution of misorientation angles for pairs of randomly selected data points ("random-pair") and the misorientation angle distribution for a random fabric ("theoretical random") (Skemer et al., 2005). The M-index ranges from 0 for random fabric to 1 for single crystal fabric. When particles of a mineral show a strong crystallographic preferred orientation, its M-index is close to 1. If the particles are heterogeneously rotated, the M-index can be close to 0. The results of PSD, microfracture density, and M-index for all 15 garnet samples are documented in Table S1.

4. Garnet fragmentation

4.1. Microstructures

Garnet microfractures in the host rocks and the "outer" shear zone (see Section 4.2) show one or more sets of preferred orientation (Figs. 3 and S1). For example, sample BB10 has one set of oriented microfractures, perpendicular to the local foliation. On the other hand, qualitatively, microfractures in the "inner" shear zone samples (see Section 4.2) show no obvious preferred orientation (Figs. 3 and S1). Garnets in the inner shear zone including the core are highly fragmented down to the submicron range and, in most cases, sheared (e.g., see samples BB16 and 41 in Fig. 3). Sheared and thus rotated fragments appear sub-angular to sub-rounded in shape. However, the fragments of sample BB12, the least sheared garnet in the inner shear zone, display little or no shear offset, thereby maintaining the original particle shape, and have angu-

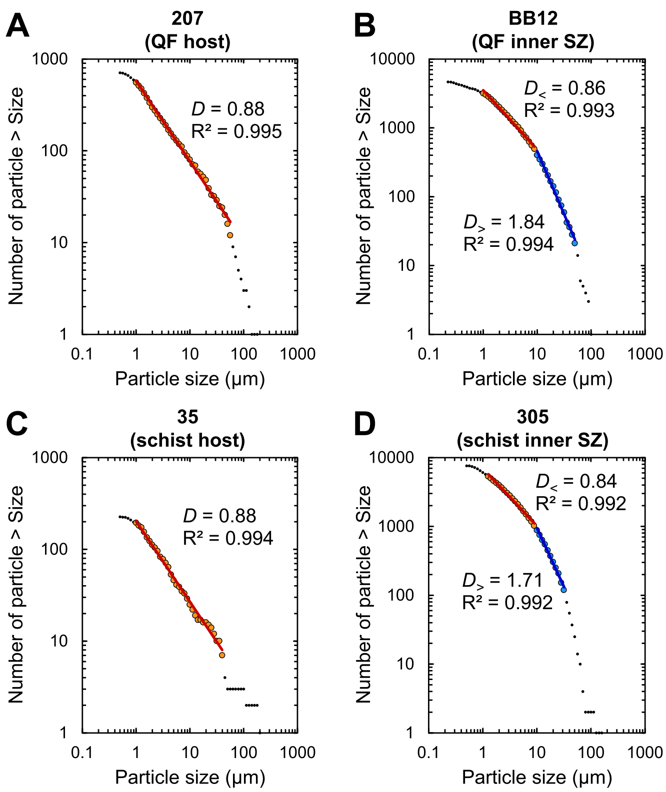

Fig. 4. Particle size distribution (PSD) results of four representative garnet samples. Cumulative size frequency distribution is plotted in log–log space against fragment diameter. Best-fit power-law lines are drawn with D-values and R^2 correlation coefficients. The host rock samples in (A) and (C) can be fit by a single power-law distribution (red lines) over more than one order of magnitude, whereas highly fragmented garnets of the inner shear zone (SZ) in (B) and (D) follow two power-law distributions (red and blue lines). Measurements from truncated data (very fine fragments) or censored data (large fragments) were excluded from the analysis (black dots). See Fig. S2 for all the analyzed garnet samples. See the online article for the color version of this figure.

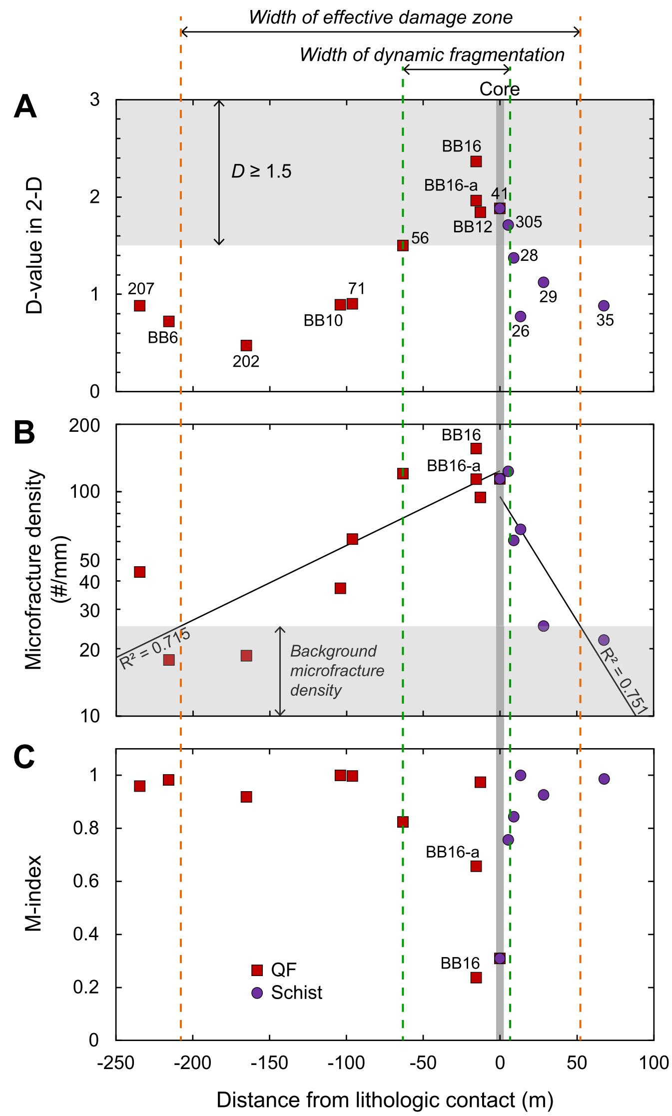

Fig. 5. Summary graphs of the analyzed data for all the fragmented garnet samples, against distance from the QF/schist lithologic contact. (A) Two-dimensional D-value plot. $D_>$ for the larger particle size is plotted where there are two power-law trends. The region of D-value ≥ 1.5, above the threshold of dynamic fragmentation, is highlighted in light gray, and the width of a dynamically fragmented zone (the inner shear zone) is determined by samples with D-value ≥ 1.5 (marked by green dashed lines). Note highly asymmetric distribution of the dynamic fragmentation zone around the shear zone core (highlighted by dark gray). (B) Microfracture density plot. Note the logarithmic scale on the y-axis. Best-fit exponential lines are drawn for two lithologic units. Background microfracture density, below the fracture density value of sample 29 (schist host), is highlighted in light gray for reference. The width of effective damage zone is determined by the best fit lines above the background microfracture density (marked by orange dashed lines). Note asymmetric distribution of the effective damage zone around the shear zone core. (C) M-index fabric intensity plot. The M-index for most samples is very high in excess of 0.8, except four samples in the inner shear zone (BB16-a, BB16, 41 and 305). Legend for the QF and schist units is displayed in (C). Sample numbers are shown in (A), and only two sample numbers at a same distance are provided in (B) and (C). See the online article for the color version of this figure.

lar, wedge-like shapes (Fig. 3). Dilatant microfractures of garnets in the SCSZ and host rocks are filled primarily with quartz and micas (locally chloritized), but include very minor quantities of feldspar, calcite, oxides, sulfides and/or phosphates (Fig. 3).

4.2. Particle size distribution, microfracture density, and fabric intensity

The cumulative PSDs of fragmented garnets from the host rocks and the outer shear zone in both the QF and schist units generally show a single power-law distribution over the majority of the size range, more than one order of magnitude, with R-square values larger than 0.99 indicating an excellent correlation (Figs. 4A, 4C and S2). Their D-values are less than 1.50, between 0.47 and 1.12 (samples 207, BB6, 202, BB10, 71, 26, 29 and 35 in Figs. 5A and S2). However, the PSDs of the inner shear zone samples do not exhibit a single power-law with a constant slope; the data are better fit by two different domains of smaller and larger particle sizes, for which we denote two D-values as $D_<$ and $D_>$, respectively (Keulen et al., 2007; see Figs. 4B, 4D and S2). The boundary between two power-law domains was chosen at a particle diameter of ∼10 μm, based on inspection of the distribution data (Table S1). In the inner shear zone, the fitted D-values for smaller fragments ($D_<$) range from 0.84 to 1.19, while the D-values for larger fragments ($D_>$) are equal to or higher than 1.50, between 1.50 and 2.36 (samples 56, BB16-a, BB16, BB12, 41 and 305 in Figs. 5A and S2). D-values in the study area (or $D_>$-values for the samples with two power-laws) tend to increase toward the shear zone core (Fig. 5A). We call the area with D- or $D_>$-values ≥ 1.5 an "inner" shear zone because of its proximity to the core, whereas the shear zone rocks with D- or $D_>$-values <1.5 are considered as "outer" shear zone. One garnet (sample 28) in the schist unit shows two power-law distributions with relatively low D-values ($D_< = 0.69$ and $D_> = 1.37$), but is considered an outer shear zone rock due to the $D_>$-value <1.5 (Fig. S2). The inner shear zone is asymmetrically distributed around the shear zone core with widths in the QF and schist units of ∼63 m and ∼5 m, respectively (Fig. 5A).

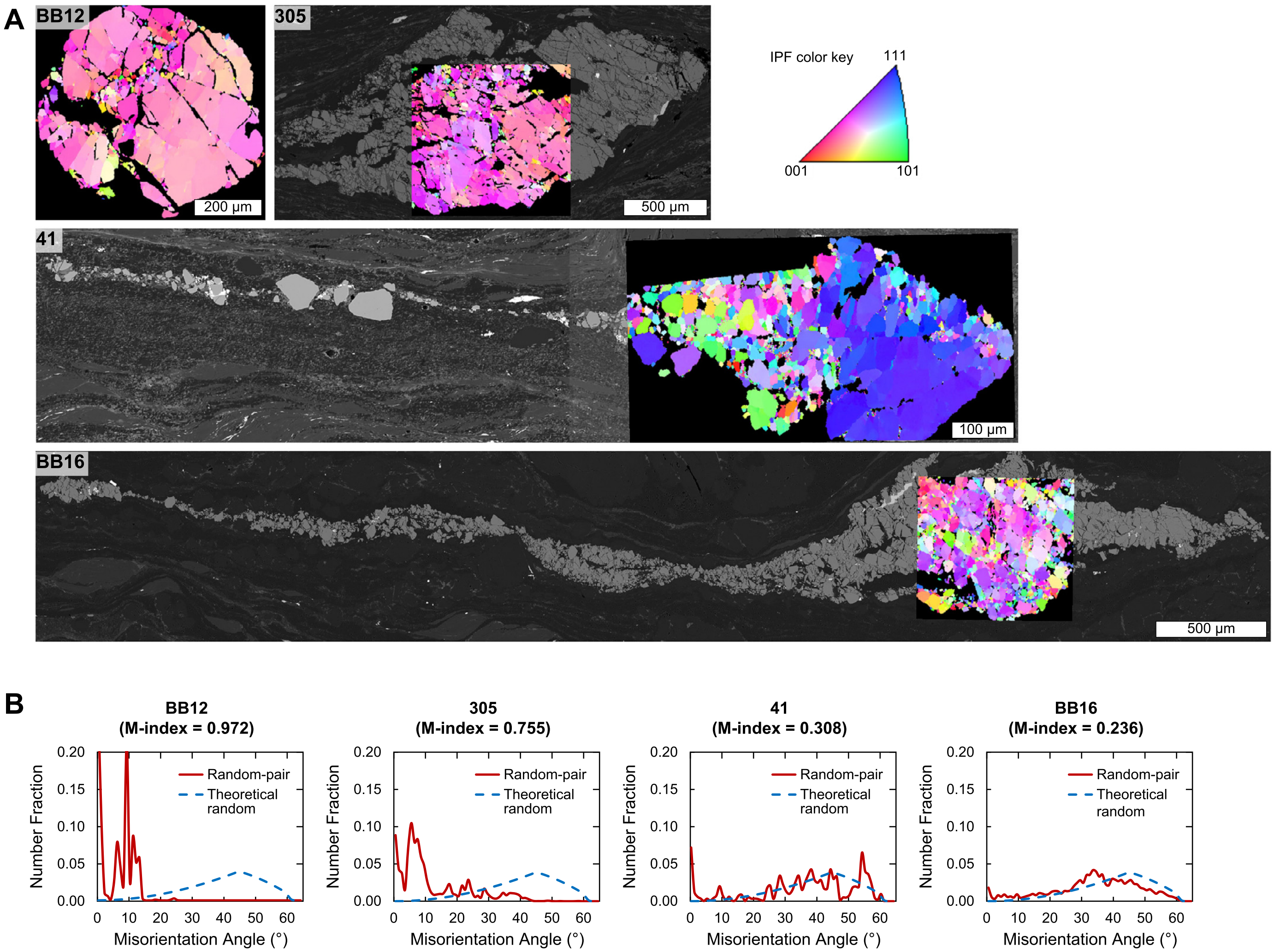

Fig. 6. Electron backscatter diffraction (EBSD) analysis for four inner shear zone samples. (A) EBSD inverse pole figure (IPF) maps of garnet showing crystal orientation aligned with Y-direction. Analyzed IPF maps are overlaid on the BSE image for each sample. The figures are arranged in order of increasing aspect ratio of fragmented garnet. (B) Misorientation angle distributions with M-index values of the analyzed IPF maps in (A). Note an inverse correlation between the aspect ratio and M-index of fragmented garnet. See the online article for the color version of this figure.

Microfracture density of fragmented garnets also generally increases toward the shear zone core from the host rocks (Fig. 5B). The host rock garnets have relatively few microfractures corresponding to microfracture density between 17.77 and 43.81 mm^{-1}. In the outer shear zone, microfracture density ranges from 18.52 to 67.71 mm^{-1}. The inner shear zone garnets show enhanced microfracture density from 94.11 mm^{-1} to 155.07 mm^{-1}. The trends of garnet microfracture density from two host rock units to the core exhibit exponential increases and also an asymmetric distribution (Fig. 5B).

The M-index fabric intensity for most garnet samples is very high exceeding 0.8, but stretched garnets in the inner shear zone show lower values (Figs. 5C and S3). The aspect ratio of fragmented garnet appears to inversely correlate with the M-index (Fig. 6). While garnets with little to no strain (e.g., sample BB12 in Fig. 6A) exhibit high M-index values close to 1 (M-index of BB12 = 0.972 in Fig. 6B), the highly stretched fragmented garnets near and in the core (e.g., samples BB16 and 41 in Fig. 6A) exhibit very low M-index values (M-index of BB16 = 0.236 and M-index of 41 = 0.308 in Fig. 6B). Relatively slightly stretched garnets such as sample 305 (Fig. 6A) in the inner shear zone show intermediate M-index values (M-index of 305 = 0.755 in Fig. 6B).

5. Discussion

5.1. Development of high *D*-values in the SCSZ

The magnitude of D is generally related to fragmentation process and energy. Hydraulic brecciation produces low D-values less than ~1.3 (Clark et al., 2006), high-energy fracturing during catastrophic explosion generates high D-value equal to or greater than 1.5 (Schoutens, 1979; Turcotte, 1986), and mature shear-related fault rocks such as gouge exhibit D-values near 1.6 predicted by the constrained comminution model (Sammis et al., 1987). Therefore, high $D_>$-values ≥1.5 of the inner shear zone garnets, similar to those reported for the explosive fragmentation, may indicate high-energy dynamic fragmentation.

Sample BB12 in the inner shear zone shows the $D_>$-value of 1.84 (Fig. 4B), which is comparable with the D-value of 1.72 for pulverized quartz from the Arima-Takatsuki Tectonic Line, Japan (Muto et al., 2015). By considering its unique damage microstructure: (1) intense fracturing, (2) angular fragments down to the micron and submicron scales (Fig. 3), and (3) a large M-index value (0.972) indicating very little to no relative fragment rotation (Fig. 6), we propose that the high $D_>$-values of QF and schist

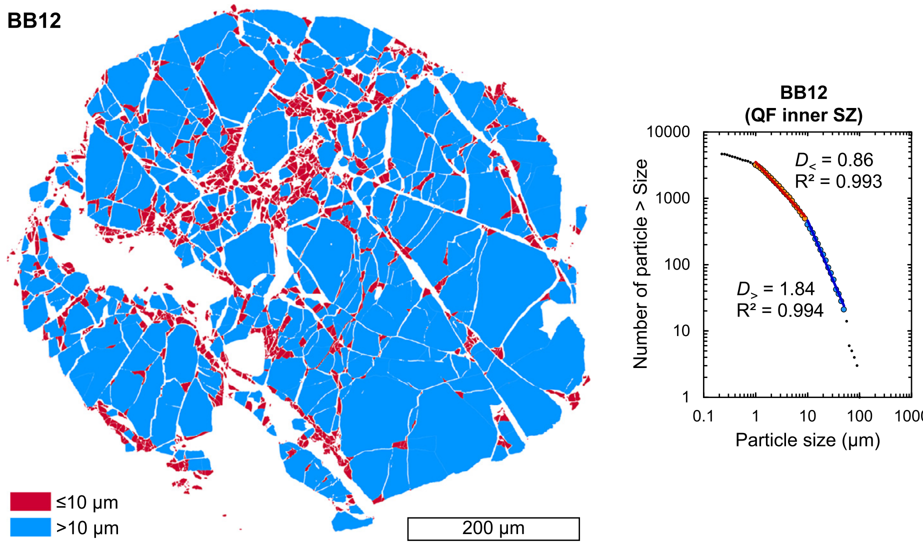

Fig. 7. Bicolor map of the processed bitmap for BB12 garnet, highlighting fragment distributions for two different size ranges with a breakpoint at 10 μm. Red and blue colors in the map indicate fragments ≤10 μm and >10 μm, respectively, corresponding to $D_<$ and $D_>$ in the PSD plot (*right panel*). The plot is taken from Fig. 4B. See the online article for the color version of this figure.

samples in and near the core reflect dynamic damage during earthquake rupture.

Sample BB16 in the XZ plane parallel to the lineation shows a $D_>$-value of 2.36 while $D_>$-value of sample BB16-a in the YZ plane is much lower (1.96) (Figs. 5A and S2). Those two samples at the same distance from the lithologic contact display distinct microstructures: sample BB16 is strongly sheared, similar to fragmented and cataclastic garnets observed by Trepmann and Stöckhert (2002), whereas sample BB16-a is relatively less deformed. $D_>$-values more than 2 were reported in naturally and experimentally produced gouge (e.g., Keulen et al., 2007) and deformed sandstone by shock recovery experiment (Buhl et al., 2013), resulting from further shear displacement (and thus more strain) and high strain rate impact. Given that only highly stretched garnet (sample BB16) shows $D_>$-value greater than 2 in the SCSZ, we suggest that postseismic viscous flow of the matrix can yield such high D-value by surface abrasion combined with rotation and cataclastic flow of the fragments (e.g., Trepmann and Stöckhert, 2002, 2003). This argument is further supported by a very low M-index value (0.236) in BB16, indicating nearly random fabric (Fig. 6). Similarly, sample 41 in the shear zone core may have experienced an increase in $D_>$-value by shear displacement as evidenced by its low M-index value (0.308) (Fig. 6).

5.2. *Insights into fragmentation processes from PSDs*

In the cumulative PSD graphs, the fragmented garnets in the inner shear zone do not show a single power-law over a large range. Instead, they show a slightly 'curved' distribution with a slope change (Figs. 4B, 4D and S2). This is not uncommon in other PSD studies on pulverized fault zone rocks (e.g., Rockwell et al., 2009; Wechsler et al., 2011). The curved distribution can be separated into two power-law regimes, with a lower D-value ($D_<$) for smaller fragments and a higher value ($D_>$) for larger fragments (Figs. 4B, 4D and S2). The power-law behavior is lost for very fine and large fragments. For the very fine fragments, this is possibly due to the resolution limit, whereas the large fragments suffer from insufficient sampling and the restriction to fragments smaller than the initial size of the garnet (Pickering et al., 1995).

The two-power-law fit has been used in a wide range of fragmentation studies including explosive magmatic fragmentation, meteoric shock and impact fragmentation, shearing comminution, and drilling comminution (e.g., Carpinteri and Pugno, 2002; Keulen et al., 2007; Roy et al., 2012; Hossain and Kruhl, 2015). Keulen et al. (2007) suggested that two power-laws with a slope change at a diameter between 1.8 and 4 μm represent the grinding limit of quartz (1.7 μm; Prasher, 1987) in shearing comminution. We calculated the grinding limit ($= 30\times(K_{IC}/H)^2$) of garnet based on crack nucleation (Hagan, 1981) using the hardness (H) and toughness (resistance to fracture, K_{IC}) of Whitney et al. (2007). Garnet has a lower limit value than quartz (0.26 μm for almandine-pyrope) and thus, in our samples, the particle size at which the slope changes is much larger (~10 μm) than the grinding limit of garnet.

Our possible explanations for the two power-law distributions in garnet include the following. First, we suggest that the change in slope is more likely related to two-stage dynamic fragmentation (Carpinteri and Pugno, 2002; Taşdemir, 2009). The primary stage is a high energy, high strain-rate volume fragmentation, typically generating coarse, through-going, wedge-shaped fragments in a 3D volume (Wittel et al., 2008). In the secondary stage, finer fragmented material forms at the surfaces of coarser fragments by low energy surface fragmentation or attrition (Carpinteri and Pugno, 2002). Sample BB12 in Fig. 7 supports these volume and surface fragmentations. Wedge-shaped coarser fragments are more spatially distributed with D-value close to 2 ($D_> = 1.84$) whereas fine fragments are concentrated between the coarser fragments with D-value close to 1 ($D_< = 0.86$) (Fig. 7). Therefore, these two power-law distributions presumably reflect a two-stage process of dynamic fragmentation mechanism (dynamic tensile fracturing and then frictional grain-boundary sliding), as reported by the experimental study of Aben et al. (2016).

The second possibility is that PSDs produced by dynamic fragmentation may be modified by chemical erosion after the fragmentation. Fracture-filling minerals are mainly quartz, micas and chlorite (Fig. 3). In the inner shear zone samples, fracture-filling biotite is partly or extensively replaced by chlorite, possibly consuming adjacent garnet. During chemical alteration, small garnet fragments along fractures can completely dissolve and disappear while large fragments experience the rounding of sharp corners and edges. The lower slope for smaller fragments is likely to reflect this chemical erosion during hydrothermal alteration. The thermal erosion model proposed by Roy et al. (2012) supports secondary post-fragmentation processes modifying the original PSD, decreasing the slope of the PSDs preferably at smaller sizes. However, even with secondary modification, it is inferred that the slope of coarser fragments ($D_>$-value) still indicates the original primary dynamic fragmentation process. We note that two power-law distributions of a garnet in the outer shear zone (sample 28) may reflect a relatively high degree of post-fragmentation modification (Fig. S2).

In addition, we also consider $D_<$- and $D_>$-values to have been produced by two different primary fragmentation processes. One process can be fluid-assisted microfracturing possibly during post- and interseismic periods, leading to the D-values close to 1, which may be the primary process that occurred in the host rock and the outer shear zone garnets. We interpret the second process to be earthquake-induced dynamic fragmentation. In this stage, more intensive fragmentation occurs within preferred size intervals ($>$ $\sim$10 μm) likely owing to high confining pressure, in agreement with the experimental evidence of Yuan et al. (2011).

Lastly, the curved distribution may be fit by a Weibull distribution (exponential-like function represented by Rosin and Rammler, 1933) generated by multiple fragmentations during successive earthquakes, instead of a single earthquake, thus showing parameters of both power-law and lognormal distributions. However, there is no clear evidence for superimposed fracture sets of different generations in the garnets we examined, nor in the other studies noted above where two different D-values were identified in single samples.

5.3. Overview of coseismic damage at FVT depths

The inner shear zone was defined as a zone with D-values $\geq$1.5, above the threshold considered to indicate high-energy fragmentation processes. We therefore attribute the $\sim$70 m-wide inner shear zone with $D \geq 1.5$ ($\sim$63 m wide in QF and $\sim$5 m in schist) to dynamic stresses generated during rupture propagation (Fig. 5A). Garnet microstructures also strongly suggest transition from non-dynamic to dynamic damage at the boundary between the outer and inner shear zones, such as considerable reduction of fragment size and changes in microfracture orientation from preferred to no apparent preferred orientations (Fig. 3).

The microfracture density that decreases with increasing distance from the QF/schist contact outlines the spatial extent of the outer effective damage zone (e.g., Mitchell and Faulkner, 2012). The microfracture density drops to the background levels at $\sim$207 m and $\sim$53 m from the contact in the QF and schist units, respectively, when background levels are taken as less than the microfracture density of sample 29 (schist host) (Fig. 5B). Sample 207 in the QF host rock shows a relatively high microfracture density, which we attribute to heterogeneous localized deformation. In the outer shear zone, fragmented garnets with microfracture density higher than the background values show D-values less than 1.5 (Figs. 5A and 5B). Therefore, damage in the outer shear zone may result from a quasi-static deformation such as hydraulic microfracturing (Clark et al., 2006).

Our interpretation based on the garnet microstructures, D-values, and microfracture density is supported by the appearance of deformed pseudotachylyte in the inner shear zone (Fig. 2). The cycles of pseudotachylyte and mylonitic deformation indicate a long history of repeated coseismic slip and post- and interseismic viscous deformation at FVT depths (e.g., Handy et al., 2007; Price et al., 2012).

6. Conclusions and implications

The SCSZ of the Norumbega fault system preserves previously undocumented characteristics of large-displacement, strike-slip faults at FVT depths. The subdivisions of the SCSZ (the host rock, the fractured outer shear zone, the dynamically fragmented inner shear zone, and the shear zone core) correlate with the pattern of damage zone around active or recently active strike-slip faults at shallow depths (e.g., Mitchell et al., 2011; Rempe et al., 2013). In the QF unit of the SCSZ, the transition from the outer to inner shear zone occurs at $\sim$63 m from the lithologic contact with prominent changes in microstructures, D-values, and microfracture densities. Such a transition is also observed across mature fault systems that are currently or recently active. For example, the boundary between fractured and pulverized zones are located at $\sim$50 m and $\sim$200 m from the fault core of the San Andreas fault and Arima-Takatsuki Tectonic Line, respectively (Mitchell et al., 2011; Rempe et al., 2013). In particular, we propose that the highly fragmented and sheared garnet near the SCSZ core (e.g., sample BB16) might correlate with the "pulverized and sheared" unit adjacent to the San Andreas fault core of Rempe et al. (2013). If this correlation is valid, then our results suggest that intense coseismic damage extends through the entire seismogenic zone in large-displacement, strike-slip faults/shear zones, although healing processes and elastic strength recovery at depth may generally render it undetectable to seismological investigations after a relatively short time (e.g., Li et al., 2006).

Although garnet is relatively abundant in the schist, it is relatively rare in the QF rocks. However, we believe that the observed microfracturing and fragmentation in garnet occurred in other mineral phases such as quartz and feldspar (Figs. 2C, 2D and 2E) during earthquake rupture. Such processes could facilitate chemical reactions and fluid-induced mineralogical changes during post- and interseismic periods. Thus, coseismic damage can affect episodic evolution of the shear zone rheology and therefore long-term weakening and strain localization of viscous deformation at depth (e.g., Handy et al., 2007). These may in turn contribute to long-term slip localization in the brittle upper crust developing along a mature seismogenic fault zone.

A final point of importance is the pronounced asymmetry of damage around the SCSZ core. While the damaged inner shear zone with $D \geq 1.5$ is $\sim$63 m wide in the QF unit (northwest side), it is $\sim$5 m wide in the schist unit (southeast side). Such asymmetric damage distribution is commonly found around active large-displacement, strike-slip faults that juxtapose rocks with dissimilar properties that form a bimaterial interface (e.g., Rockwell et al., 2009; Mitchell et al., 2011; Rempe et al., 2013). Dynamic rupture models have shown that bimaterial faults can host ruptures with preferred direction, producing more pronounced damage on the stiffer side (e.g., Dalguer and Day, 2009; Xu and Ben-Zion, 2017). If the strong asymmetry of damage in the SCSZ reflects rupture dynamics, then the right-lateral slip along the shear zone would indicate southwest preferred directivity of rupture propagation in the area. The asymmetric damage observed in the SCSZ exhumed from FVT depths may imply that the same damage processes of seismogenic strike-slip faults occurring in the uppermost crust operate through the entire seismogenic zone.

Declaration of competing interest

The authors declare that they have no known competing financial interests or personal relationships that could have appeared to influence the work reported in this paper.

Acknowledgements

We thank Tom Mitchell and an anonymous reviewer for helpful comments that improved the manuscript. This research was supported by National Science Foundation grants EAR-0820946, EAR-1347087 and EAR-1727090. B.R. Song was supported in part by a Michael J. Eckardt Dissertation Fellowship from the University of Maine.

Appendix A. Supplementary material

Supplementary material related to this article can be found online at https://doi.org/10.1016/j.epsl.2020.116226.

References

Aben, F.M., Doan, M.-L., Gratier, J.-P., Renard, F., 2017. Coseismic damage generation and pulverization in fault zones. In: Thomas, M.Y., Mitchell, T.M., Bhat, H.S. (Eds.), Fault Zone Dynamic Processes. American Geophysical Union, pp. 47–80.

Aben, F.M., Doan, M.-L., Mitchell, T.M., Toussaint, R., Reuschlé, T., Fondriest, M., Gratier, J.P., Renard, F., 2016. Dynamic fracturing by successive coseismic loadings leads to pulverization in active fault zones. J. Geophys. Res., Solid Earth 121, 2338–2360. https://doi.org/10.1002/2015JB012542.

Anders, M.H., Wiltschko, D.V., 1994. Microfracturing, paleostress and the growth of faults. J. Struct. Geol. 16, 795–815. https://doi.org/10.1016/0191-8141(94)90146-5.

Ben-Zion, Y., Zaliapin, I., 2019. Spatial variations of rock damage production by earthquakes in southern California. Earth Planet. Sci. Lett. 512, 184–193. https://doi.org/10.1016/j.epsl.2019.02.006.

Buhl, E., Kowitz, A., Elbeshausen, D., Sommer, F., Dresen, G., Poelchau, M.H., Reimold, W.U., Schmitt, R.T., Kenkmann, T., 2013. Particle size distribution and strain rate attenuation in hypervelocity impact and shock recovery experiments. J. Struct. Geol. 56, 20–33. https://doi.org/10.1016/j.jsg.2013.08.007.

Carpinteri, A., Pugno, N., 2002. A fractal comminution approach to evaluate the drilling energy dissipation. Int. J. Numer. Anal. Methods Geomech. 26, 499–513. https://doi.org/10.1002/nag.209.

Clark, C., Schmidt Mumm, A., Collins, A.S., 2006. A coupled micro- and macrostructural approach to the analysis of fluid induced brecciation, Curnamona Province, South Australia. J. Struct. Geol. 28, 745–761. https://doi.org/10.1016/j.jsg.2006.01.005.

Cochran, E.S., Li, Y.-G., Shearer, P.M., Barbot, S., Fialko, Y., Vidale, J.E., 2009. Seismic and geodetic evidence for extensive, long-lived fault damage zones. Geology 37, 315–318. https://doi.org/10.1130/G25306A.1.

Dalguer, L.A., Day, S.M., 2009. Asymmetric rupture of large aspect-ratio faults at bimaterial interface in 3D. Geophys. Res. Lett. 36, L23307. https://doi.org/10.1029/2009GL040303.

Hagan, J.T., 1981. Impossibility of fragmenting small particles: brittle-ductile transition. J. Mater. Sci. 16, 2909–2911. https://doi.org/10.1007/BF02402857.

Handy, M.R., Hirth, G., Bürgmann, R., 2007. Continental fault structure and rheology from the frictional-to-viscous transition downward. In: Handy, M.R., Hirth, G., Hovius, N. (Eds.), Tectonic Faults: Agents of Change on a Dynamic Earth. The MIT Press, pp. 139–182.

Harris, R.A., Day, S.M., 1997. Effects of a low-velocity zone on a dynamic rupture. Bull. Seismol. Soc. Am. 87, 1267–1280.

Hossain, M.D.S., Kruhl, J.H., 2015. Fractal geometry-based quantification of shock-induced rock fragmentation in and around an impact crater. Pure Appl. Geophys. 172, 2009–2023. https://doi.org/10.1007/s00024-014-0922-8.

Huang, Y., Ampuero, J.-P., Helmberger, D.V., 2014. Earthquake ruptures modulated by waves in damaged fault zones. J. Geophys. Res., Solid Earth 119, 3133–3154. https://doi.org/10.1002/2013JB010724.

Incel, S., Schubnel, A., Renner, J., John, T., Labrousse, L., Hilairet, N., Freeman, H., Wang, Y., Renard, F., Jamtveit, B., 2019. Experimental evidence for wall-rock pulverization during dynamic rupture at ultra-high pressure conditions. Earth Planet. Sci. Lett. 528, 115832. https://doi.org/10.1016/j.epsl.2019.115832.

Jamtveit, B., Petley-Ragan, A., Incel, S., Dunkel, K.G., Aupart, C., Austrheim, H., Corfu, F., Menegon, L., Renard, F., 2019. The effects of earthquakes and fluids on the metamorphism of the lower continental crust. J. Geophys. Res., Solid Earth 124, 7725–7755. https://doi.org/10.1029/2018JB016461.

Ji, S., Zhao, P., Saruwatari, K., 1997. Fracturing of garnet crystals in anisotropic metamorphic rocks during uplift. J. Struct. Geol. 19, 603–620. https://doi.org/10.1016/S0191-8141(97)00006-0.

Johnson, S.E., Lenferink, H.J., Price, N.A., Marsh, J.H., Koons, P.O., West, D.P., Beane, R., 2009. Clast-based kinematic vorticity gauges: the effects of slip at matrix/clast interfaces. J. Struct. Geol. 31, 1322–1339. https://doi.org/10.1016/j.jsg.2009.07.008.

Keulen, N., Heilbronner, R., Stünitz, H., Boullier, A.-M., Ito, H., 2007. Grain size distributions of fault rocks: a comparison between experimentally and naturally deformed granitoids. J. Struct. Geol. 29, 1282–1300. https://doi.org/10.1016/j.jsg.2007.04.003.

Li, Y.-G., Chen, P., Cochran, E.S., Vidale, J.E., Burdette, T., 2006. Seismic evidence for rock damage and healing on the San Andreas fault associated with the 2004 M 6.0 Parkfield earthquake. Bull. Seismol. Soc. Am. 96, 349–363. https://doi.org/10.1785/0120050803.

Lockner, D.A., Walsh, J.B., Byerlee, J.D., 1977. Changes in seismic velocity and attenuation during deformation of granite. J. Geophys. Res. 82, 5374–5378. https://doi.org/10.1029/jb082i033p05374.

Mandelbrot, B.B., 1982. The Fractal Geometry of Nature. W. H. Freeman, San Francisco.

Mitchell, T.M., Ben-Zion, Y., Shimamoto, T., 2011. Pulverized fault rocks and damage asymmetry along the Arima-Takatsuki Tectonic Line, Japan. Earth Planet. Sci. Lett. 308, 284–297. https://doi.org/10.1016/j.epsl.2011.04.023.

Mitchell, T.M., Faulkner, D.R., 2012. Towards quantifying the matrix permeability of fault damage zones in low porosity rocks. Earth Planet. Sci. Lett. 339–340, 24–31. https://doi.org/10.1016/j.epsl.2012.05.014.

Morton, N., Girty, G.H., Rockwell, T.K., 2012. Fault zone architecture of the San Jacinto fault zone in Horse Canyon, southern California: a model for focused post-seismic fluid flow and heat transfer in the shallow crust. Earth Planet. Sci. Lett. 329–330, 71–83. https://doi.org/10.1016/j.epsl.2012.02.013.

Muto, J., Nakatani, T., Nishikawa, O., Nagahama, H., 2015. Fractal particle size distribution of pulverized fault rocks as a function of distance from the fault core. Geophys. Res. Lett. 42, 3811–3819. https://doi.org/10.1002/2015GL064026.

Pickering, G., Bull, J.M., Sanderson, D.J., 1995. Sampling power-law distributions. Tectonophysics 248, 1–20. https://doi.org/10.1016/0040-1951(95)00030-Q.

Prasher, C.L., 1987. Crushing and Grinding Process Handbook. Wiley, New York.

Price, N.A., Johnson, S.E., Gerbi, C.C., West, D.P., 2012. Identifying deformed pseudotachylyte and its influence on the strength and evolution of a crustal shear zone at the base of the seismogenic zone. Tectonophysics 518–521, 63–83. https://doi.org/10.1016/j.tecto.2011.11.011.

Price, N.A., Song, W.J., Johnson, S.E., Gerbi, C.C., Beane, R.J., West, D.P., 2016. Recrystallization fabrics of sheared quartz veins with a strong pre-existing crystallographic preferred orientation from a seismogenic shear zone. Tectonophysics 682, 214–236. https://doi.org/10.1016/j.tecto.2016.05.030.

Rempe, M., Mitchell, T., Renner, J., Nippress, S., Ben-Zion, Y., Rockwell, T., 2013. Damage and seismic velocity structure of pulverized rocks near the San Andreas Fault. J. Geophys. Res., Solid Earth 118, 2813–2831. https://doi.org/10.1002/jgrb.50184.

Rockwell, T., Sisk, M., Girty, G., Dor, O., Wechsler, N., Ben-Zion, Y., 2009. Chemical and physical characteristics of pulverized Tejon Lookout granite adjacent to the San Andreas and Garlock faults: implications for earthquake physics. Pure Appl. Geophys. 166, 1725–1746. https://doi.org/10.1007/s00024-009-0514-1.

Rosin, P., Rammler, E., 1933. The laws governing the fineness of powdered coal. J. Inst. Fuel 7, 29–36.

Roy, S.G., Johnson, S.E., Koons, P.O., Jin, Z., 2012. Fractal analysis and thermal-elastic modeling of a subvolcanic magmatic breccia: the role of post-fragmentation partial melting and thermal fracture in clast size distributions. Geochem. Geophys. Geosyst. 13, Q05009. https://doi.org/10.1029/2011GC004018.

Sagy, A., Korngreen, D., 2012. Dynamic branched fractures in pulverized rocks from a deep borehole. Geology 40, 799–802. https://doi.org/10.1130/G33194.1.

Sammis, C., King, G., Biegel, R., 1987. The kinematics of gouge deformation. Pure Appl. Geophys. 125, 777–812. https://doi.org/10.1007/BF00878033.

Schoutens, J.E., 1979. Nuclear Geoplosics Sourcebook. Volume IV. Part II. Empirical Analysis of Nuclear and High-Explosive Cratering and Ejecta. Defense Nuclear Agency.

Skemer, P., Katayama, I., Jiang, Z., Karato, S.-I., 2005. The misorientation index: development of a new method for calculating the strength of lattice-preferred orientation. Tectonophysics 411, 157–167. https://doi.org/10.1016/j.tecto.2005.08.023.

Soda, Y., Okudaira, T., 2018. Microstructural evidence for the deep pulverization in a lower crustal meta-anorthosite. Terra Nova 30, 399–405. https://doi.org/10.1111/ter.12355.

Spudich, P., Olsen, K.B., 2001. Fault zone amplified waves as a possible seismic hazard along the Calaveras fault in central California. Geophys. Res. Lett. 28, 2533–2536. https://doi.org/10.1029/2000GL011902.

Sullivan, W.A., Peterman, E.M., 2017. Pulverized granite at the brittle-ductile transition: an example from the Kellyland fault zone, eastern Maine, U.S.A. J. Struct. Geol. 101, 109–123. https://doi.org/10.1016/j.jsg.2017.07.002.

Taşdemir, A., 2009. Fractal evaluation of particle size distributions of chromites in different comminution environments. Miner. Eng. 22, 156–167. https://doi.org/10.1016/j.mineng.2008.06.002.

Trepmann, C.A., Stöckhert, B., 2002. Cataclastic deformation of garnet: a record of synseismic loading and postseismic creep. J. Struct. Geol. 24, 1845–1856. https://doi.org/10.1016/S0191-8141(02)00004-4.

Trepmann, C.A., Stöckhert, B., 2003. Quartz microstructures developed during non-steady state plastic flow at rapidly decaying stress and strain rate. J. Struct. Geol. 25, 2035–2051. https://doi.org/10.1016/S0191-8141(03)00073-7.

Trepmann, C.A., Stöckhert, B., Dorner, D., Moghadam, R.H., Küster, M., Röller, K., 2007. Simulating coseismic deformation of quartz in the middle crust and fabric evolution during postseismic stress relaxation - an experimental study. Tectonophysics 442, 83–104. https://doi.org/10.1016/j.tecto.2007.05.005.

Turcotte, D.L., 1986. Fractals and fragmentation. J. Geophys. Res. 91, 1921–1926. https://doi.org/10.1029/JB091iB02p01921.

Walsh, J.B., 1965. The effect of cracks on the compressibility of rock. J. Geophys. Res. 70, 381–389. https://doi.org/10.1029/jz070i002p00381.

Wechsler, N., Allen, E.E., Rockwell, T.K., Girty, G., Chester, J.S., Ben-Zion, Y., 2011. Characterization of pulverized granitoids in a shallow core along the San Andreas Fault, Littlerock, CA. Geophys. J. Int. 186, 401–417. https://doi.org/10.1111/j.1365-246X.2011.05059.x.

Whitney, D.L., Broz, M., Cook, R.F., 2007. Hardness, toughness, and modulus of some common metamorphic minerals. Am. Mineral. 92, 281–288. https://doi.org/10.2138/am.2007.2212.

Wittel, F.K., Carmona, H.A., Kun, F., Herrmann, H.J., 2008. Mechanisms in impact fragmentation. Int. J. Fract. 154, 105–117. https://doi.org/10.1007/s10704-008-9267-6.

Xu, S., Ben-Zion, Y., 2017. Theoretical constraints on dynamic pulverization of fault zone rocks. Geophys. J. Int. 209, 282–296. https://doi.org/10.1093/gji/ggx033.

Yuan, F., Prakash, V., Tullis, T., 2011. Origin of pulverized rocks during earthquake fault rupture. J. Geophys. Res., Solid Earth 116, B06309. https://doi.org/10.1029/2010JB007721.